IEEE Access
Multidisciplinary ⋮ Rapid Review ⋮ Open Access Journal

Received 8 August 2022, accepted 22 August 2022, date of publication 9 September 2022, date of current version 19 September 2022.

Digital Object Identifier 10.1109/ACCESS.2022.3202925

RESEARCH ARTICLE

Dual-Slot Cavity Antenna for mm-Wave Beamforming Array

RAJVEER S. BRAR, (Graduate Student Member, IEEE), AND RODNEY G. VAUGHAN, (Life Fellow, IEEE)

Sierra Wireless Mobile Communications Laboratory, School of Engineering Science, Simon Fraser University, Burnaby, BC V5A 1S6, Canada

Corresponding author: Rajveer S. Brar (rsbrar@sfu.ca)

This work was supported by the Natural Sciences and Engineering Research Council of Canada under Grant NSERC-2022-05376.

ABSTRACT A cavity-fed, dual-slot element and its 4-element linear array configurations for beam-steering applications at 28 GHz are described. The element cavity is formed from rectangular substrate integrated waveguide (SIW), perturbed at one of its corners to excite dual slots for increasing the impedance bandwidth. With a mobile terminal in mind, we look to both classical array principles and to the available theories for finite arrays with mutual coupling, to help guide the design. The impact of the finite ground-plane required to support the slot elements and array is investigated by simulation, including the impact on the patterns of using a cellphone chassis as a platform. A chassis-born 4-element (8 slots) configuration, suitable for beamforming in 28 GHz 5G networks is demonstrated for both linear polarizations. The simulation results are supported by pattern measurements of prototypes, a challenging task at 28 GHz.

INDEX TERMS Cavity resonator, slot antennas, 28GHz, phased arrays.

I. BACKGROUND AND INTRODUCTION

A. SLOT ELEMENT BASICS

Slot arrays are important due to their conformability to the surface of a platform such as the chassis of a cellphone. Slot elements are relatively easy to fabricate and integrate with feeds interfacing to front-end electronics. The slot is often viewed as a dual of the traditional dipole, with its impedance estimated from the metal dipole by Babinet's principle e.g., [1]. Like short dipoles, single-mode slots are typically a half-wavelength long, and they have their highest feed-point resistance at the center of the slot, tapering to zero at the ends of the slot which are short-circuited. For a 50-ohm feed, a direct across-slot feed can be off-center in order to impedance match. Wideband designs with a direct feed across the slot are also available, e.g., [2]. For integration of the antenna to a surface, feeding via the cavity is preferred to a direct across-slot feed.

The remainder of this section is a concise literature review of the relevant technologies for our design, and our contribution. The references are representative only, it is not possible to cite all the significant contributions.

The associate editor coordinating the review of this manuscript and approving it for publication was Bilal Khawaja.

B. CAVITY SLOT DESIGN

Using Babinet's principle to get slot admittances from the impedance of its complementary antenna, the metallic strip dipole, was verified in the classic 1972 paper by Long [3]. Long also studied the impedance of a slot terminating a TE_{01} waveguide of different lengths, demonstrating that an electrically small cavity-depth (i.e., waveguide length) was feasible for efficient radiation. In our design below, we use a cavity depth of a quarter wavelength because such a configuration can readily match to 50 ohms. Theoretical and measured impedance characteristics of multiple slots on cavity waveguides were studied in 1980 by Paoloni [4], and design procedures for waveguide slot arrays were published by Elliot, e.g., [5], and for various applications in several later publications, e.g., [6]. However, for beamforming (as opposed to fixed-beam designs), the elements must have individual cavities for independent control of the excitation.

C. BEAM FORMING ARRAYS

Recent designs for multiple cavity-fed slot antennas for beamforming are now summarized. In [7], orthogonally polarized, 2-element arrays at 2.5 GHz were realized using orthogonally oriented slots on adjacent cavities arranged as a

2 by 2 array. Diagonally offset cavities had the same polarization, with mutual coupling claimed to be reduced by using mushroom-type structures.

Different operating frequencies require different technologies. For 28/38 GHz dual-bandwidths, the design of [8] used an etched, shaped parasitic patch above the slot. Also at 28 GHz, there are published designs using direct-fed patches, aperture-fed patches, Vivaldi, and Yagi-Uda antennas, e.g., [9] and [10].

For MIMO communications, antenna performance metrics are the envelope correlation coefficient and diversity gain, eg., [11]. For phased arrays, the usual metric is array antenna gain in the beam-steered directions. In both cases, the total active reflection coefficient defines a limit on impedance bandwidth. Whereas phased arrays use deterministic (from the beam direction) phase shifts, MIMO systems adapt random phases and amplitudes resulting from the random multipath. The differences between phased arrays and MIMO-type antennas are elaborated in [10].

D. PHASED ARRAYS ON CELLPHONE CHASSIS

Normally, for a mobile terminal, the signals from arrays, or strictly speaking, from multi-element-antennas, are diversity-combined for MIMO communications. The signal-to-interference-plus-noise, in multipath, ie., without reference to a physical direction, can be maximized. Phased arrays maximize gain to a physical direction, suited to line-of-sight situations such as single-room indoor cell scenarios.

Using mmWave frequencies, prototype phased arrays have previously been mounted inside a cellphone chassis. Such arrays can experience blockage to the field-of-view caused by the shape of the metal frame. For example, in [12], a Vivaldi antenna array used parasitic metal strips on a bezel to avert severe beam blockage. In [13], a dual-polarized cavity-backed slot antenna array inside the chassis of a cellphone offered 52% coverage (100% coverage is the full sphere) for a beamformed gain of more than 5 dBi, when holding the mobile phone in a hand. In call mode (cellphone beside the head, see Figure 1a), the hand can block an antenna mounted on a lateral bezel [14], while in data mode (cellphone held in two hands), the hands can block the antenna on the bottom bezel.

In [15], a cavity-fed slot array fed with a stepped coax probe is mounted on the side bezel of a metallic cellphone chassis, enabling fan beamforming. The presence of a hand over the side bezel can degrade the gain by 5-7 dB [15]. Another approach [16] uses parasitic elements with controllable reactive terminations for what is essentially a phased array but fed by a single monopole on a SIW feedline. Placing this array on the side bezel makes its gain sensitive to its location along the lateral bezel. Placing it at the center of the bezel was reported to provide the highest gain (as a standalone structure). In [17], the antenna is located internal to the metallic chassis but behind holes (c.f., slots) in the chassis to allow radiation.

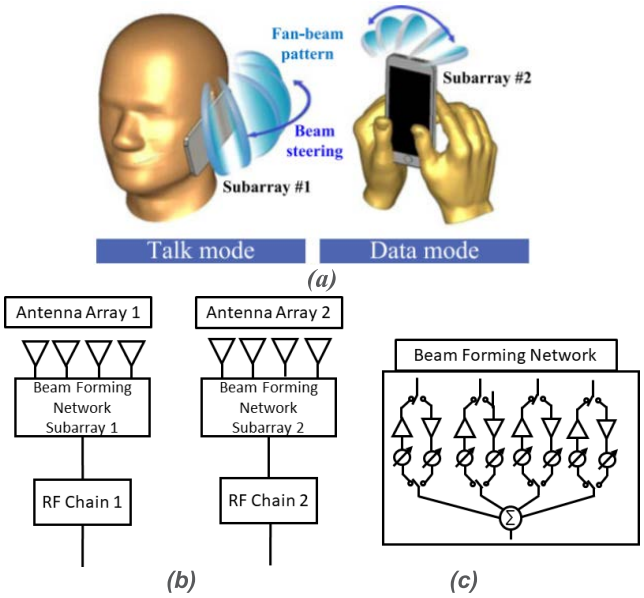

FIGURE 1. (a) talk mode and data mode for a cellphone terminal. (Reproduced from [19] with permission). (b) depiction of a hybrid beamformer where the subarray beamformer is analogue and each RF chain is digitized for digital beamforming; (c) depiction of switching for the time domain duplexing.

At higher frequencies such as mmWaves, the Friis path gain decreases, and to compensate, higher antenna gains are sought. This requires arrays, but the associated cost of extra RF chains becomes significant. Therefore, hybrid beamforming has been developed, where subarrays are beamformed using analog phase shifters, and only the subarrays (as opposed to all the elements) have a dedicated RF chain for digital beamforming. This is depicted in Figures 1b and 1c, where the analog beamforming uses standardized time-domain duplexing to share transceiver resources. By using low-loss analog stages, hybrid beamforming is reported in [18] to attain the communications performance of fully digital beamforming, with significant cost savings on the RF hardware.

E. CONTRIBUTIONS

The new contributions of this paper include:

- a new element and array design for the 28 GHz 5G band for cellphone mounting. Its advantage is its ease of manufacture due to its PCB design (operating through an aperture in a metallic chassis, illustrated below) and its enhanced bandwidth from using an extra slot as part of the element. Previous designs required more expensive multiple layer PCBs for realizing patches with parasitic elements.
- A demonstration that the array theory based excess directivity (viz., above that corresponding to simply the number of array elements) is not available for the finite arrays of interest here. This is because, in practice, the embedded element patterns are too dissimilar from each other.

- A comparison of the available theories for including the effects of mutual coupling in a finite array. We demonstrate that only one of these theories works well for the finite arrays that can fit on a cellphone chassis.

The rest of this paper is laid out as follows. Section II reviews the impact of mutual coupling in array design, as it applies to our array which has a small, finite ground-plane. Section III presents the antenna element design and Section IV presents our results for a cavity-backed slot array. A comparison of our design with those of other papers is provided in Section V, and Section VI concludes the paper.

II. THEORIES FOR FINITE ARRAYS

Classical array theory is where the array factor and a common element pattern multiply to give the array antenna pattern. Such a formulation seldom holds accurately for finite arrays on a finite platform. This is because a finite array normally has significantly different embedded element patterns, so there is no common element pattern. Below, the notations from the original references are used rather than unifying the terminology.

The pattern of a finite array is found from the electric field transmitted to a location $\boldsymbol{r}$ by reference to a far-field (of the array) distance, R, as, eg., [20, p.14],

$$\boldsymbol{E}(\boldsymbol{r}) = \frac{e^{-jk_0R}}{R}\sum_i a_i \boldsymbol{f}_i(\theta,\phi)\, e^{jk\boldsymbol{r_i}.\hat{r}} \tag{1}$$

where in this notation, $\boldsymbol{E}$ is the electric field vector in the direction of the $\boldsymbol{r}$ vector (cartesian form: $\boldsymbol{r} = R\sin\theta\cos\phi\hat{x} + R\sin\theta\sin\phi\hat{y} + R\cos\theta\hat{z}$), k is the scalar free space propagation constant, R is a far-field distance from the array (i.e., the field point must not only be in the far-field of the element, but also in the far field of the array), λ is wavelength, a_i is the complex excitation vector, $\hat{r}$ is unit vector in the direction of $\boldsymbol{r}$, $\boldsymbol{r_i}$ is the position vector of the i^{th} element, and $\boldsymbol{f}_i$ is the embedded far-field pattern of the i^{th} antenna element, defined here as its directional response in the presence of the other elements all terminated (typically in 50 ohms) and mounted on the finite platform. This choice means that the effects of the mutual coupling and the finite ground-plane are included in the element patterns. The dependencies in (1) can be expressed as $\boldsymbol{E}(r,\theta,\phi)$, with the scalar r dropping out in the far-field pattern description.

The mutual coupling between elements is an array antenna parameter, and as such it does not change with the different element excitations. It is preferably described using the impedance matrix of a multiport antenna because a single fixed coefficient (eg., Z_{12}) describes the network coupling between ports 1 and 2. The signal coupling between two elements in general requires more than just one scattering coefficient (eg., S_{12}) – it also requires S_{11} and S_{22}. The matrices $\boldsymbol{Z}$ and $\boldsymbol{S}$ are related by $\boldsymbol{Z} = Z_0(\boldsymbol{I}\text{-}\boldsymbol{S})^{-1}(\boldsymbol{I}+\boldsymbol{S})$, so S_{12} can represent the coupling for well-matched ports.

Changes to the embedded element pattern, relative to its isolated pattern, were demonstrated by Pozar [21] for dipoles. These dipoles have no ground-plane, i.e., there is no finite ground-plane effect. But a ground-plane is required for slot arrays, and its edges can affect the element patterns. Electrically small wire dipoles can be approximated by canonical minimum scattering antennas (MSAs) which simplifies their modelling. A property of MSAs is that their transmit pattern is the same as their scattering pattern, so this makes it clear that a slot supported by a ground-plane cannot be an MSA. However, this does not mean that slot elements cannot have other MSA-like properties. In any event, for a small (ie., finite) ground-plane bearing slot elements, the ground-plane edge diffraction impacts the embedded patterns significantly. To better understand the pattern behavior of a finite array, antenna array pattern changes against variations of the ground-plane size are investigated here.

The impedance bandwidth of an array is governed by its active reflection coefficient [21] (this includes the effects of mutual coupling, the excitations, and a finite ground-plane for a slot or other element types). The bandwidth also depends on the beam-steering direction since it depends on the excitations. It is known that with mutual coupling and/or a finite ground-plane, the resulting pattern maximum is, in general, not the same as the direction of the steering vector.

The situation for a planar array is as follows. The notation from [21] is maintained here. Consider a rectangular grid with M elements (columns) along the x-axis with physical spacing a, and N elements (rows) along the y axis with spacing b, so that there are $K = MN$ elements. Placing the elements in a single row and using index $k = 1; 2; 3; \ldots K$, then $i_k = k \bmod M$ is the x index (column) of element k and $j_k = 1 + \text{int}((k\text{-}1)/M)$ is the y index (row) of element k. Let $u = k_0 a\sin\theta\cos\phi$ *and* $v = k_0 b\sin\theta\sin\phi$ relate to the usual directional cosines in terms of the scalar propagation constant (in this notation, k_0), with (u_0, v_0) relating to the steering angle. Then the active reflection coefficient of the m^{th} (from 1 to K) element is [21]

$$\Gamma_m(\theta_0,\phi_0) = \sum_{n=1}^{K} S_{mn} e^{-j[(i_n-j_m)u_0+(j_n-j_m)v_0]} \tag{2}$$

where S_{mn} is the scattering parameter between the m^{th} and n^{th} elements, and the integer terms such as $(j_n - j_m)$ index the spacing beween the elements. The field of the embedded m^{th} element is related to its isolated far-field pattern, $F(\theta,\phi)$ (recall that all the elements themselves may be identical but their embedded patterns are likely different owing to mutual coupling and finite ground-plane effects), as

$$E_m^e(r;\theta,\phi) = F(\theta,\phi)\frac{e^{-jk_0r}}{r} V_0[e^{j(i_m-1)u+j(j_m-1)v} + \sum_{n=1}^{K} S_{mn} e^{j[(i_n-1)u+(j_n-1)v]}] \tag{3}$$

where in this terminology, V_0 is the active element excitation with the other elements are terminated and not excited.

In the array far-field at scalar distance $|\mathbf{r}| = r$, the field transmitted from the array is the weighted sum of these (likely-different) embedded element fields. For the intended

beam-steered direction (u_0, v_0), this is [21, eq. (15)]

$$E^a(r,\theta,\phi) = F(\theta,\phi)\frac{e^{-jk_0 r}}{r}V_0\sum_{n=1}^{K}[e^{-j(i_n-1)u_0-j(j_n-1)v_0} + \sum_{m=1}^{N}S_{mn}e^{-j[(i_m-1)u_0+(j_m-1)v_0]}] \times e^{j[(i_n-1)u+(j_n-1)v]} \quad (4)$$

In a modification [22] to this formulation, the *isolated* element pattern, $F(\theta,\phi)$, was replaced with the *embedded* element pattern of the central element in finite large array. This pattern can be readily found by simulation by using periodic boundary conditions making it appear to be an infinite lattice.

It is emphasized that this is for all (isolated) elements which are identical and identically oriented in an infinite lattice, i.e., classical array theory. It is not likely to hold for a practical, finite array of slots having a finite ground plane.

To demonstrate the differences between these theories for our array design (Section III), below we find an isolated element pattern by simulation, and use the above equation to find an array antenna pattern to compare it with simulations of a finite array.

More recently, Abdallah and Wasylkiwskyj [23] presented a new finite array formulation which uses the embedded element pattern of each element *with the remaining elements open-circuited*. The notation from [23] is maintained here. The n^{th} embedded element pattern, *for when the other elements are (variously) loaded*, for a linear array along the z-axis, is [23]

$$F_n(\theta,\phi) = \sum_{m=1}^{N}(Z_{mn}+Z_{gm})R_{gm}^{-\frac{1}{2}}Y_{mn}^{a}R_{gn}^{\frac{1}{2}}F_m^0(\theta,\phi) \quad (5)$$

where $F_m^0(\theta,\phi)$ is the open circuit embedded element pattern of the m^{th} element, Z_{gm} is the impedance of the voltage generator driving the m^{th} element, Z_{mn} is the $(m,n)^{\text{th}}$ element of the array antenna impedance matrix, and Y_{mn}^a is the $(m,n)^{\text{th}}$ element of a matrix containing elements $(Z_{mn}+Z_{gm}\delta_{mn})$ and inversed, where δ_{mn} is a Kronecker delta and $R_{gn} = \text{Real}Z_{gn}$. So $F_n(\theta,\phi) = F_n^0(\theta,\phi)$ if there is no mutual coupling. The antenna array pattern is calculated from the weighted sum of these embedded element patterns.

We now consider simple dipole arrays as a vehicle to assess the differences between the different formulations, given that the dipole arrays have no finite ground-plane effects.

A. SMALL ARRAY OF ACTIVE DIPOLES

Figure 2 shows the array of four lossless dipoles (z-oriented) with a comparison of the pattern results. The dipoles resonate (in isolation) at 27.5 GHz, have a radius of $0.01\lambda_0$, and for a 50 ohm load (so not likely to be a perfect match to the dipole), the single-element impedance bandwidth for $|S_{11}|$ <-10 dB is 9% (26.5-29 GHz). The embedded-element bandwidth does not change much for this case because the elements are reasonably well-spaced ($0.5\lambda_0$) and so the mutual coupling is reasonably low. Figure 2 includes the pattern results from (4) for the two cases:

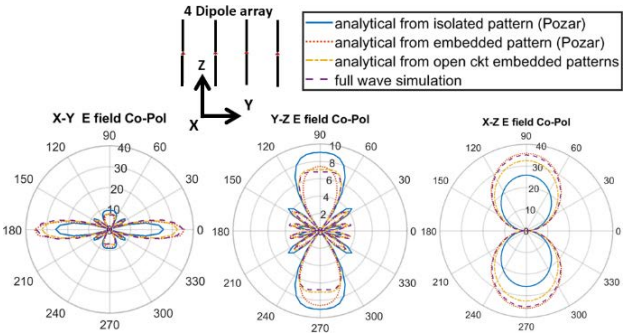

FIGURE 2. E-field array pattern cuts (in V/m at $r = 1$m) of 4-element dipole array with all excitations the same (and no ground-plane). Simulated patterns are compared to the cases of: (4) [21]; (4) modified [22]; and (5).

(i) using the isolated pattern of an element, ie., in the absence of any other element [21];

(ii) using the embedded element pattern from an infinite array lattice [22], here simulated using periodic boundary conditions at specified inter-element distances.

For the 4-element array of wire dipoles, the array response from (4) is not very close to simulation results for case (i), but for case (ii) - when using the modified form of [22] - it is extremely close. Equation (5) is also extremely close.

Using (4) with the isolated element pattern (case (i) above) is not useful here because it does not account for the scattering from the adjacent elements, i.e., the mutual coupling. In Section III, we also compare these approaches for slot elements, and it will be seen that only (5) works well.

B. SMALL ARRAY USING PARASITIC DIPOLES

We now investigate the impact on the array antenna pattern of a mutually coupled parasitic scatterer (a proximate dipole, short-circuited). In a numerical experiment, two short-circuited dipoles are equi-spaced from an active dipole (all z-oriented). A spacing of $0.5\lambda_0$ creates more broadside gain than the stand-alone dipole, shown in figure 3(a). For spacings closer than $0.5\lambda_0$ the gain increases in the end-fire directions as in Yagi-Uda antennas, and this reduces the broadside gain. When the spacing is more than λ_0, the main lobe splits; e.g., at $1.5\lambda_0$, the main lobe is split into 2 symmetric lobes, and at $2\lambda_0$ spacing, the main lobe is split into 3 lobes, following classical array theory. The number of lobes increases with the spacing but ultimately converges back to a dipole-like pattern for large spacing where the mutual coupling that excites the parasitic dipoles becomes negligible.

In another experiment, two parasitic dipoles at the ends of a 4-element active dipole array, with fixed $0.5\lambda_0$ spacing, is investigated, see Figure 3(b). For a spacing to the parasitics of $0.5\lambda_0$, the broadside gain is reduced by 0.1 dB, with a 1 dB higher sidelobe level in the endfire directions. When these

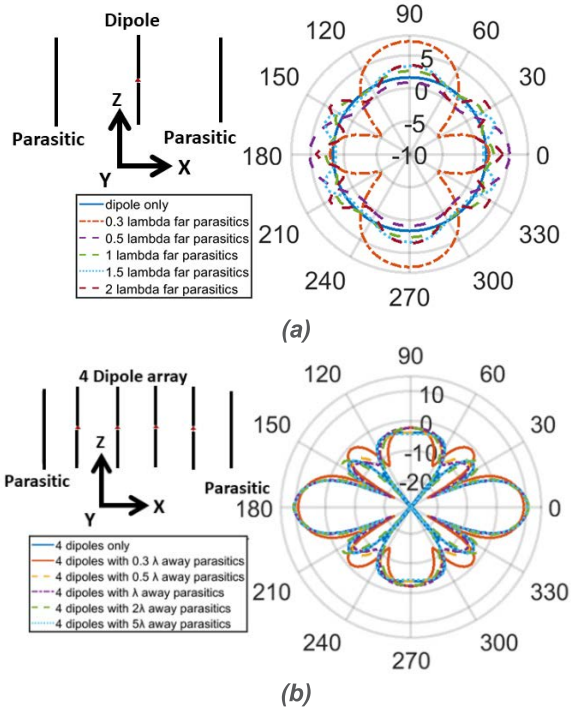

FIGURE 3. Simulated gain (in dBi) plots of the (x-y) pattern cut. (a) single excited dipole with two shorted dipole scatterers; (b) 4-element dipole array with shorted dipole scatterers adjacent to the outer array elements.

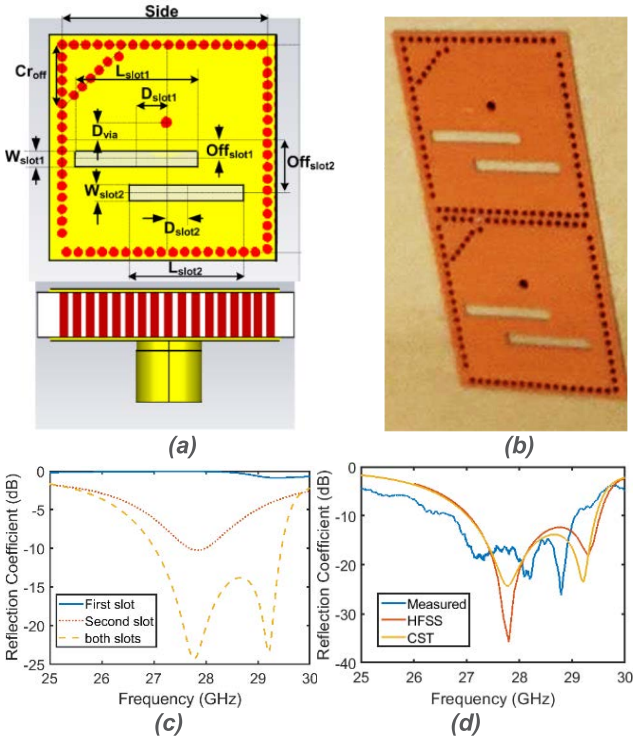

FIGURE 4. (a) Geometry of the SIW CBS antenna, with dimensions in mm: Side = 6.5, Cr_{off} = 2,L_{slot1} = 3.9, D_{slot1} = 0.85, W_{slot1} = 0.5, Off_{slot1} = 0.44, L_{slot2} = 3.7, D_{slot2} = 0.75, W_{slot2} = 0.5, Off_{slot2} = 1.54, D_{via} = 0.76; (b) top view of 2 element fabricated prototype (c) reflection coefficient for the individual and combined slots; (d) simulation and measured reflection coefficient.

parasitic dipoles are spaced by λ_0 and $2\lambda_0$ from the outer array elements, the broadside gain increases by 0.2 dB and 0.4 dB, respectively. If we view the parasitic scattering as akin to the diffraction scattering of a ground-plane edge in slots arrays, then a finite ground-plane or platform edges can act to either slightly decrease or increase the antenna gain, i.e., the finite ground-plane size can be used as a design parameter.

These experiments demonstrate the likely impact of nearby scatterers such as chassis edges or other finite ground-plane edges on embedded element patterns and array antenna patterns. An analytic model of a finite array in [24] uses diffraction to model ground-plane edges showing how the diffraction effect is more significant in smaller arrays than larger arrays. But the diffraction contributions for all directions become too complicated with ground-plane corners, so simulation or physical measurement is normally required for accurate estimation of the embedded element patterns.

Using (5) also results in a close match for our cavity-backed slot antenna arrays on a finite ground-plane, confirming (5) as useful for designs such as ours presented here. The details of these results are in Section IV.

III. CAVITY BACKED SLOT ELEMENT DESIGN

Our design has dual slots for each element, see Figure 4a. These slots are of different lengths (and of course locations, but both are close to the TE_{120} cavity mode maxima) and act to improve the cavity-fed element impedance bandwidth through coupled resonances, as shown in Figure 4b. It is seen that the individual slots behave differently to their combined presence. The corner trim perturbs the TE_{120} mode so that the different length slots are both still close to the field maxima. Another view is that the closely spaced slots strongly mutually couple.

The dual resonances in the impedance are shown in Figure 4c. This type of design has no simple analytic model, it is most conveniently solved by simulation. The configuration here is hand-optimized (by parametric study, not shown here, and good enough for reaching diminished returns) for impedance bandwidth, and so no formal optimization was used here. The vias are standard sizes for cost-effective PCB manufacturing, viz., 12 mils diameter, and there is a 10 mil spacing between adjacent via edges. The cavity (PCB substrate) is Rogers 6002 with a specified 1.524 mm thickness, real dielectric constant of 2.94, and a loss tangent of 0.0012 at 10 GHz which has a modified value at other frequencies (see below).

The simulated and measured results show good impedance bandwidth, shown in Figure 4c, viz., the simulated impedance bandwidth is 9% ($|S_{11}| < -10$ dB for 27-29.5 GHz) and the measured impedance bandwidth is 8.2% ($|S_{11}| < -10$ dB for 26.7-29 GHz). The different approaches of HFSS and CST simulations agree reasonably well except for regions of low S_{11}. The differences between measurement and simulation

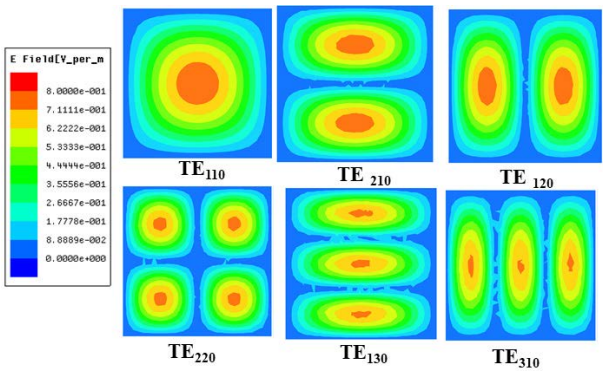

FIGURE 5. Cavity mode resonance frequencies and field structure of the dielectric-filled lossless (no slots) cavity. The shading represents the strength of the electric field between the top and bottom plates.

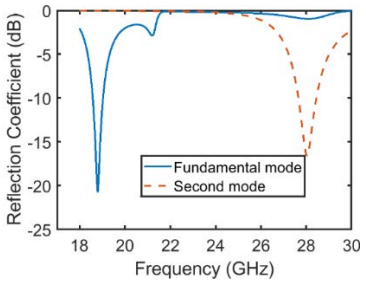

FIGURE 6. Simulated reflection coefficient of cavity-backed slot antennas for two resonance modes fed by a coaxial probe (HFSS).

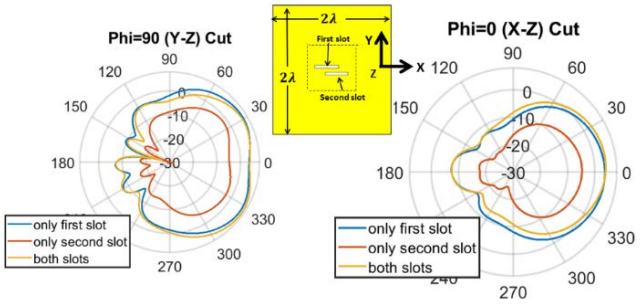

FIGURE 7. Simulated gain patterns (in dBi) of dual slot antenna element at 28GHz, with a $2\lambda \times 2\lambda$ ground-plane, excited with a single coax probe. There is a gain reduction resulting from using only the second slot (normally parasitic), where the dielectric losses come to the fore.

results are mainly due to the different configurations being assessed. Important factors include: the electrical properties of dielectrics are seldom verified with high accuracy; the feed detail (especially the feed cable); and the physical inaccuracy of prototypes, e.g., even professionally manufactured prototypes may have been realized with different batches of substrate having a slightly different complex permittivity. For an array, the element impedance bandwidth must often be at least twice the required impedance bandwidth specified, because of the bandwidth-reducing (relative to a single element) metric of the total active impedance bandwidth [11].

The radiating slots effectively create a lossy cavity situation, and it is of interest to model this. The simplest model is a lossless cavity, which has cavity resonances at, eg., [25],

$$f_e = \frac{c}{2\pi\sqrt{\mu_r \epsilon_r}}\sqrt{\left(\frac{m\pi}{a}\right)^2 + \left(\frac{n\pi}{b}\right)^2 + \left(\frac{l\pi}{h}\right)^2} \qquad (6)$$

where f_e denotes the eigenmode frequency, ϵ_r and μ_r are the purely real (because it is lossless) anisotropic relative permittivity and permeability of the substrate, c is the speed of light in free space, and m, n, l refer to the integer numbers of variations in the standing wave pattern along the x-, y- and z-axis directions, respectively. In HFSS, the eigenmodes of a lossless cavity correspond to ''resonant'' frequencies and modal field distributions. (Here we take maximum modal dominance to mean resonance, but strictly, in electrical circuits, resonance refers to a port impedance being purely real.) For a square cavity, the fundamental mode TE_{110} resonates at 19 GHz, the degenerate TE_{120} and TE_{210} modes at 30 GHz, and the even higher order modes, e.g., TE_{220} at 38 GHz, and TE_{130}/TE_{310} at 43 GHz. The well-known electric field intensity forms are in Figure 5 for the first few modes.

By placing the slot radiator at a field maximum, the mode maximally radiates. Using a coaxial probe, the first mode (TE_{110}, 19 GHz) has a 2.5% impedance bandwidth ($|S_{11}| < -10$ dB for 18.5 -19 GHz); and the second mode (TE_{120}, 28 GHz) has a 2.8% impedance bandwidth ($|S_{11}| < -10$ dB for 27.6 to 28.4 GHz), as shown in Figure 6. The probe location governs the matching for a particular resonance mode or sum of modes.

Figure 7 gives simulated gain pattern cuts for the dual slot element on a finite ground plane ($2\lambda_0 \times 2\lambda_0$). The maximum gain is 7.24 dBi at 28 GHz, at directions away from broadside. The main lobe is -36^0 from zenith in the E- plane (y-z), and this is due to the slot element being away from the center of the finite ground plane. With a single slot only (the second slot is completely short-circuited), the maximum gain drops to 6.28 dBi and its direction is -35^0 from zenith in the E-plane. With the second slot only, there are two lobes formed and their maximum gains are -1.7 dBi and -2.5 dBi at -37^0, 35^0 respectively, from zenith in the E-plane. These values are low because the second slot by itself has poor radiation efficiency since the cavity losses dominate the radiation losses.

In Figure 8 for the dual slot element, we see increasing maximum gain with frequency until 29.5 GHz. Beyond 29.5 GHz, the main lobe starts to split into two lobes and the maximum gain begins to decrease.

The radiation efficiency is a maximum of -0.18 dB at 28 GHz and drops for higher frequencies as the ohmic losses increases with frequency. But below 28 GHz, the radiation efficiency *decreases* with decreasing frequency. This is because of the decreasing radiation resistance of a slot with decreasing electrical length. An important point here is that the simulator (here CST) uses general dispersion models to accurately extrapolate dielectric properties (i.e., loss tangents) at various frequencies for the materials that

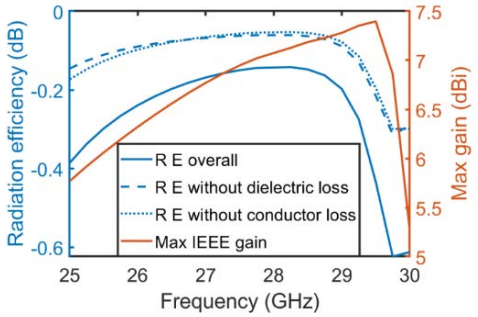

FIGURE 8. Radiation efficiency and maximum gain (direction not included) of the dual slot antenna element. The radiation efficiency drops after 28GHz because the ohmic losses of the cavity increase, and also drops with decreasing frequency because of the decreasing radiation resistance of a slot with decreasing electrical length. The gain drops steeply after 29.5GHz because the pattern splits into dual lobes.

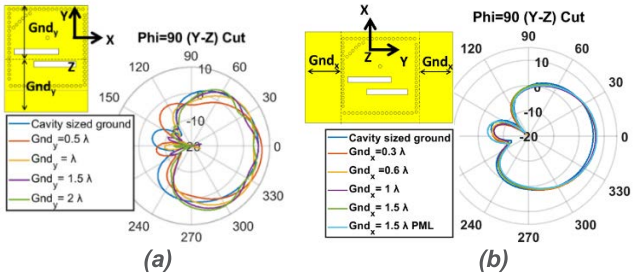

FIGURE 9. Simulated gain patterns (in dBi) of the dual-slot element on the finite-sized ground plane. (a) The E-plane pattern ripples are from the edge diffraction sources interfering with the slot's direct radiation, and decrease as the E-plane ground-plane gets bigger. (b) The H-plane ground-plane edge diffractions are less because these edges are illuminated less.

are characterized by a single frequency. Here, the dielectric material is characterized for 10GHz, but we are running it at 28GHz. From the 10 GHz specification, the dispersion model within CST gives a loss tangent at this 28 GHz of 0.003528. With this, the dielectric losses are similar to the conductor losses.

The finite ground-plane is known to cause ripples in the patterns, eg., [26], from edge diffractions which interfere with the slot radiation contributions. The phase difference between the contributions of the diffraction and the slot(s) depend on their spacing. Also, an increasing distance between the ground edge and the slot weakens the diffraction source, eg., [27].

Figure 9 shows the element patterns in the E-Plane for various ground-plane sizes. The cavity size (minimum ground-plane size) is $0.7\lambda_0$ along the E-plane and $0.7\lambda_0$ along the H-plane, and this can be seen in (a). The zenith gain is 5.6 dBi. By increasing the ground-plane size along the E-plane to λ_0 (only in the negative y-direction, see Figure 9a), the broadside gain increases to 6.9 dBi, and this is the maximum for any E-plane ground-plane size where the H-plane ground-plane size is kept to $0.7\ \lambda_0$.

Extending the E-plane ground-plane to $\text{Gnd}_y = \lambda_0$ (Figure 9a) acts to split the main lobe as expected, reducing

TABLE 1. E-Plane ground-plane edge effect on broadside gain for H-plane ground-plane spacing size of 0.7λ.

Gnd_y (λ_0)	Gain at zenith for a dual-slot element, for various spacings to the E-plane ground-plane edge (dBi)	Gain at zenith for dipole with parasitics at the same spacings (dBi)
0.5	6.9	5.2
1.0	3.7	2.8
1.5	5.7	1.3
2.0	3.7	4.2

the zenith gain to 3.7 dBi. For $\text{Gnd}_y = 1.5\lambda_0$, the lobes re-align in the zenith direction giving a gain of 5.6 dBi. For $\text{Gnd}_y = 2\lambda_0$, the beam again splits into 2 lobes. These results are summarized in terms of broadside gain in Table 1. This behavior is different to that of a dipole with parasitic dipoles where, for example, a spacing of $1.5\lambda_0$ acts to split the beam, and the maximum zenith gain occurs for a spacing of λ_0 or $2\lambda_0$. Thus, the scattering from parasitic dipoles, while having a mechanism akin to the diffraction from ground-plane edges, has a different impact on the pattern, and this is simply because dipole scattering sources are different to the diffraction sources at the same spacing, particularly in their phases.

Extending the ground-plane size along the H-plane from the original cavity size by 0.3 λ_0 (shown as Gnd_x in Figure 9b - note that this is different to Figure 9a) improves the peak gain from 5.6 dBi to 6.9 dBi. (Note that the peak is not quite at zero degrees in this *y-z* cut.) Any further increase in this spacing to the edge does not increase this peak gain. In summary, the edge plane diffraction sources cannot, unfortunately, be readily modelled using the simpler case of scattering dipoles with the same spacings.

IV. PHASED ARRAY BEHAVIOUR

This section looks at classical array factor directivity whose interesting behavior can guide the initial design of an array. We also compare the array theories from Section II to simulated results for our dual slot array design.

A. ARRAY FACTOR DIRECTIVITY

A two-element array of omnidirectional sources without mutual coupling has maximum broadside directivity at an element spacing of about $0.7\ \lambda_0$, calculated from its array factor [28] (p.589, note the error in the labeling of the boresight and endfire cases). For the array factor usage to be accurate requires all the embedded element patterns to be identical and have no mutual coupling. Figure 10 shows the basic results for a 4- element array, as considered in this paper. The directivity of an array antenna is the usual

$$D(\theta, \phi) = \frac{4\pi\ |AF(\theta, \phi) f\ (\theta, \phi)|^2}{P_{total}} \tag{7}$$

where P_{total} is the total radiated power from the array. An $N = 4$ element array normally has an expected gain increase of $N = 4$, i.e., 6dB. But here all the

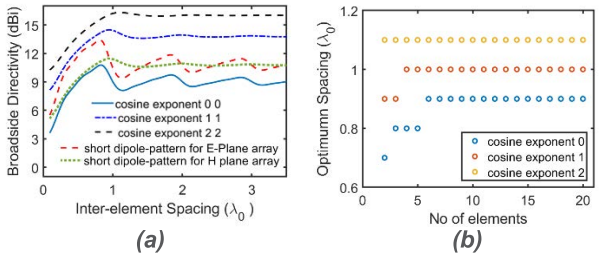

FIGURE 10. (a) Broadside classical array directivity against element spacing for a uniformly spaced 4-element linear array where all element patterns are modelled by a "double cosine" power pattern, $(cos^{2n}(\theta)cos^{2m}(\phi))$, radiating in a hemisphere (infinite ground-plane). The zero exponents case is an idealized omnidirectional element. The array antenna directivity assumes no mutual coupling. (b) Inter-element spacing for maximum directivity for different sizes of a linear array against the number of elements, for the different element pattern models.

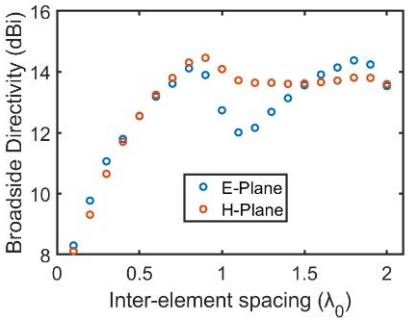

FIGURE 11. Broadside directivity vs inter-element spacing for identical element patterns from the dual-slot element. The maximum directivity for E-plane array and H-plane array occurs at an inter-element spacing of $0.8\lambda_0$ and $0.9\lambda_0$ respectively.

radiation is confined to a hemisphere, so there is an extra 3dB. For hemispheric-isotropic elements, the broadside array antenna directivity oscillates with the spacing, but approaches (6+3) dBi for large N.

From Figure 10(a), for a 4-element array of isotropic elements, the array antenna directivity in a hemisphere has a maximum of 10.7 dBi for an element spacing of $0.8\lambda_0$. The array action adds 7.7 dB to the hemispheric element directivity of 3 dBi. For the 2-element array, this spacing for maximum directivity is $0.7\lambda_0$. For this isotropic element case, only the array factor governs the optimum spacings. But for directive elements, it is perhaps not widely understood that the element pattern, featured in (7), also impacts the optimum element spacing for maximum broadside directivity, meaning that the array directivity cannot be separated from the element directivity.

For a directive element pattern model using exponents $n = m = 1$, the maximum array antenna directivity of 14.5 dBi is for a spacing of 0.9 λ_0. This changing spacing for maximum array antenna directivity is from the element patterns acting to suppress grating lobes. The 4-element array action for this spacing adds 6.7 dB to the element directivity of 7.8 dBi.

The dipole-like pattern model in a hemisphere, ($m = 0$, $n = 1$), has element directivity of 4.7 dBi and a resulting 4-element E-plane array antenna directivity of 13.3 dBi at the optimum spacing of 0.8 λ_0. For an H-plane array with this element, the maximum directivity is 11.5 dBi for a spacing of 0.9 λ_0. So the excess directivity (meaning above the expected 6 dB for a 4 element array) is 2.6 dB and 0.8 dB for the E-plane and H-plane arrays, respectively. Note that these are for scalar, or purely-polarized element pattern models, so there are no cross-polar components in the directivity calculation.

For the cosine pattern model with ($m = n = 2$), the element directivity is 10 dBi, and the array antenna gain is 16.3 dBi. The array action adds 6.3 dB. This excess directivity (here above 6 dB) decreases for more directive elements.

Figure 10(b) shows that the number of elements in the array also governs the optimal spacing. For example, increasing N from 2 to 6, the spacing for maximum array antenna directivity (with isotropic elements) increases from 0.7 λ_0 to 0.9 λ_0, and further increasing number of elements does not change this optimum spacing (for maximum directivity). It is emphasized that this is for no mutual coupling. Similarly, for elements having a pattern with ($m = n = 1$), this optimum spacing for maximum array antenna directivity changes to λ_0 for a 4-element array. More directive elements (eg., having exponents of $m = n = 2$) have the same optimum spacing regardless of the number of elements in the array. In summary, this behavior is a starting point for configuring an array for maximum directivity, before the impact of mutual coupling is included. However, the narrower beamwidth of more directive elements also means a smaller scan angle range. The tradeoff between array gain and scan range also guides the spacing choice.

The above behavior of directivity with element spacing for classical arrays is useful for a first cut array design. But the classical array formulation relies on there being no mutual coupling and having identical element patterns, both of which are unlikely in practice. The question arises, are our element patterns sufficiently similar, and is the mutual coupling sufficiently low, to harness the excess gain available from the classical array antenna directivity?

To check if such excess directivity is available from a realistic embedded element pattern, we used a simulated embedded dual-slot inner element pattern from our 4-element array, for all the elements of a 4-element array. Again, this is for co-polarization only. The cross-polarization is lower than the co-polarization by 35 dB at broadside. Figure 11 shows the broadside directivity for our dual-slot element arrays. The element directivity is 7.5dBi. For the E-plane array, the element spacing for the first maxima of directivity is 0.8 λ_0 (there is another maxima at 1.8 λ_0 which in fact has 0.2 dB higher directivity). For the H-plane array, the spacing is 0.9 λ_0. The directivities of the array antennas are 14.0 dBi and 14.5 dBi respectively. i.e., there is 0.5 dB and 1 dB excess directivity. The trend looks similar to the dipole pattern for the E-plane and H-plane arrays in Figure 10a, but the

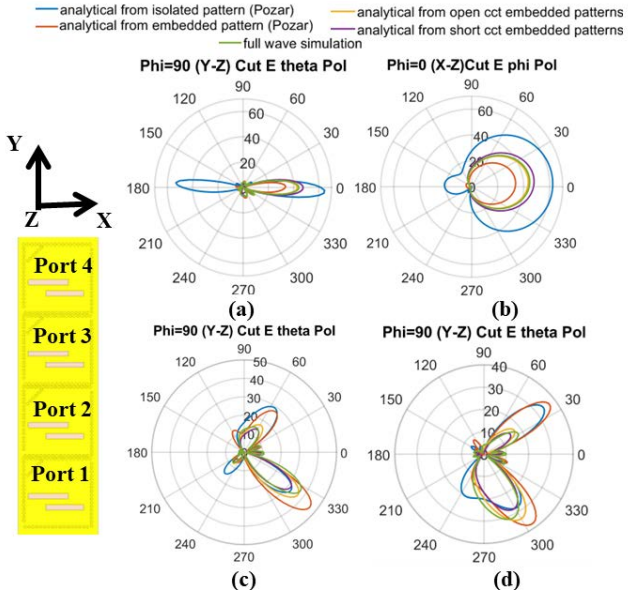

FIGURE 12. E-field pattern cuts (in V/m) of the dual slot, 4-element antenna array for the geometry depicted on the left. (a) and (b) are the cuts through the broadside direction; (c) beam steered to - 40^0; (d) beam steered to 40^0. These simulations agree well with the results of (5).

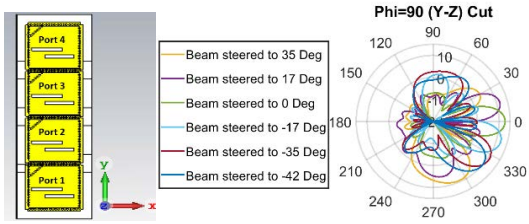

FIGURE 13. 4 element linear E-plane array geometry and simulated gain patterns (in dBi) in the E-plane cut (Y-Z plane).

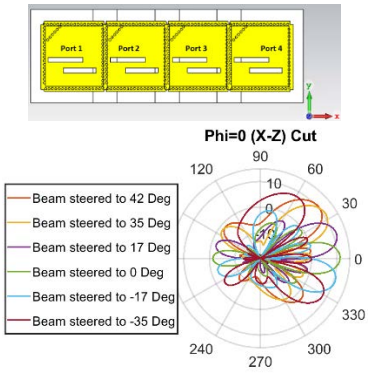

FIGURE 14. H-plane 4 element linear array geometry, and beam-steered patterns (simulated gain in dBi from simulated element patterns) for the H-plane cut ($x - z$ plane), using phase-alignment at broadside.

excess directivity falls well short of the 2.6 dB when using the modelled element patterns.

So from classical array considerations, there appears to be excess directivity available from the array action when using one of our embedded element patterns, and taking all the embedded element patterns to be the same. In practice, this does not happen because the actual element patterns are too different from each other. Also, there will be grating lobes in the field-of-view (where we want to able to scan) for these element spacings. As a design trade-off between maximum directivity (spacing 0.8 λ_0 for the first maxima of broadside directivity of the array antenna) and +/- 90^o scan range without grating lobes (spacing of 0.5 λ_0), we chose a spacing of 0.65 λ_0 for the E-plane and H-plane arrays. This spacing is also a minimum here because it corresponds to the cavity size.

For our dual-slot elements (with spacing $0.65\lambda_0$) the mutual coupling is about -17 dB between adjacent E-plane elements and about -20 dB between adjacent H-plane elements (not shown here), which is low enough to be negligible for practical considerations (also not shown here).

B. FINITE ARRAYS: 4-ELEMENT E-PLANE ARRAY

The two finite array theories are now tested for the 4-element dual-slot antenna array. The patterns are in Figure 12 as linearly scaled, with units Volts/m at $r = 1$. The results from (4) are not a good fit to accurate simulations, even for the modified case of using an embedded element pattern. But the model of (5) is in good agreement with the simulation results. This demonstrates that for experimental array antenna results, we must either use all of the measured embedded element patterns in a summation, as per (1), or the model of (5), in order to get accurate estimates of the array antenna patterns.

Patterns from the E-plane array are depicted in Figure 13. The array has embedded antenna element gains of 6.3, 7.5, 7.5, 7.5 dBi, respectively, for ports 1 to 4. The asymmetry of the gains between the two outer elements, is from the different geometry of the outer elements relative to their adjacent ground-plane edges.

These embedded element patterns are now co-phased at their broadside directions and added (by computer calculation, so there is no physical combiner here as part of the antenna) and this results in an array antenna gain of 12.9 dBi with sidelobe levels of -12.6 dB relative to the main lobe. The direction of the maximum beam-formed gain is less than the angle expected from the geometric beam direction of classical array theory, viz., the intended beam is steering to 20^0 and 40^0, instead of steering to 17^0 and 35^0, respectively. The 3dB scan coverage is from $+30^0$ to -45^0. This is for the element patterns which are co-phased at broadside and then geometric phase shifts used to steer the beam. The phase difference between element patterns at angles within their 3dB beamwidths is now negligible. So, broadside phase alignment is sufficient for 3dB scan coverage without significant loss of gain. Beyond these angles, grating lobes emerge. The asymmetric scan range is also due to the different embedded element patterns.

C. H-PLANE ARRAY

The H-plane array configuration is shown in Figure 14. The element patterns are again combined in-phase (by computer)

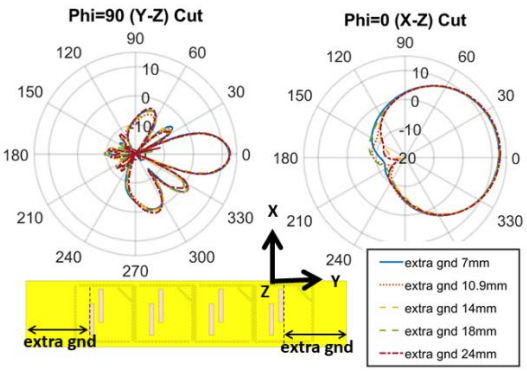

FIGURE 15. Simulated gain patterns (in dBi) in the E-plane cut ($y-z$ plane) and H- plane cut ($x-z$ plane) for a 4 element E-plane linear array. The patterns are all essentially the same showing the very minor impact of the truncation of the ground-plane at the ends of the array.

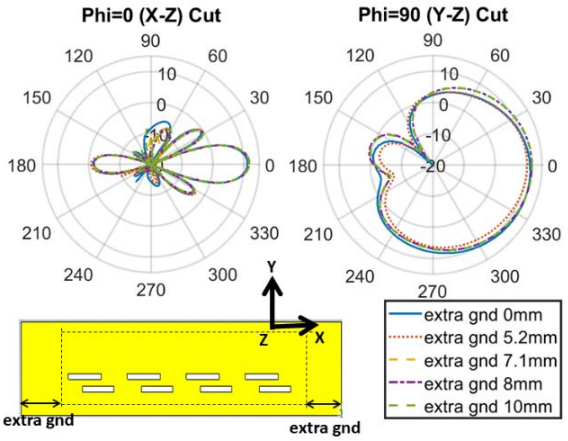

FIGURE 16. Effect of ground-plane extent in the H-plane: simulated gain patterns (in dBi) in the H-plane cut ($x-z$) and E plane ($y-z$) for a 4 element H-plane linear array.

to give the array broadside radiation. The embedded elements have broadside gains of 5.4 dBi, 5.3 dBi, 5.4 dBi, and 5 dBi for ports 1 to 4, respectively. They also have different and asymmetric patterns. The beam-formed pattern has a broadside gain of 11.2 dBi with the first sidelobes down by 12 dB. When beam-steered to $+45^0$, still with the element patterns co-phased at broadside, the array gain reduces to 10.4 dBi, and a grating lobe appears at 7.9 dB below the main beam gain. The 3 dB scan coverage is $+55^0$ to -35^0, and beyond these angles, a grating lobe dominates.

D. IMPACT OF ARRAY GROUND-PLANE LENGTH

The impact on the pattern of the E-plane array is shown in Figure 15. If the ground-plane is extended in the E-plane from its original minimum size (the cavity size), then the array pattern remains the same except for small changes in sidelobe levels and backlobe levels. This is different to the isolated element pattern which changes with ground plane size in the E-plane as depicted in Figure 7, and this is simply because for the case of antenna array, the inner elements do not have diffracting edges. The ground-plane size in the E-plane is a parameter of Figure 15, to demonstrate its minor impact.

Figure 16 demonstrates the negligible impact of the ground-plane extent in the H-plane. (However, in the E-plane (y-z), the y-plane extent acts to skew the main lobe.) On increasing the ground plane by $extra\ gnd = 0.5\lambda_0$ (see Figure 16), the broadside gain of the main lobe increases by 0.5 dB. However, it does not increase further. This trend is like the one seen in Figure 9 for single antenna element.

E. PATTERN MEASUREMENTS

The embedded element patterns of antenna ports are measured in our NSI near field chamber, see Figure 17a. One port is excited while all other ports are loaded with 50 Ω terminations. The cylindrical near field synthetic aperture is formed by rotating the antenna under test (AUT) through 360^0 in azimuth (y-z plane) with the probe (WR34) moving in elevation along the x-axis of the AUT. The AUT is mounted on a polyester foam slab. The IF bandwidth of receiver is set to 300 Hz as a trade-off between noise performance and measurement speed. The peak SNR in the near field aperture is around 50dB. The limited aperture in the x-axis (the maximum x-direction aperture length in our chamber is 1.5 meters) corresponds to a limit of only $\pm 25^0$ in the elevation plane scan - see Figure 17a. Mostly, mmWave antenna terminals are tested using over-the-air systems which do not separate the performance of the various components such as the receiver sensitivity, communications signal processing algorithms, and, in particular, the antenna performance. Measuring patterns is challenging at these frequencies.

TABLE 2. Measured broadside embedded element total gain.

Array	Port number and its total gain in dBi			
	1	2	3	4
H plane	3.7	5	5.2	2.2
E plane	2	5.8	5.1	6

In a pattern measurement, the total gain is typically measured, and it is left to the user to calculate the (IEEE) gain. However, our elements are all well-matched and so the matching loss is negligible, leaving cable losses which are removed in the calibration process. For both simulation and measurement, the embedded element patterns are computer-combined in this paper. It is emphasized that there is no physical combining circuit in the array antenna here.

Figures 17 (b-c) show simulated and measured embedded element patterns (port 2) of the H-plane array. The finite ground plane acts to change the beam direction in the E-plane (y-z), as discussed above. Figures 17 (d-e) show the embedded element pattern of port 4 of the E-plane array. All the other measured embedded patterns are omitted for brevity, but each of the embedded element boresight gains are listed in Table 2.

The measured azimuth cuts of (b) and (d) are not a close match between simulation and measurement in the

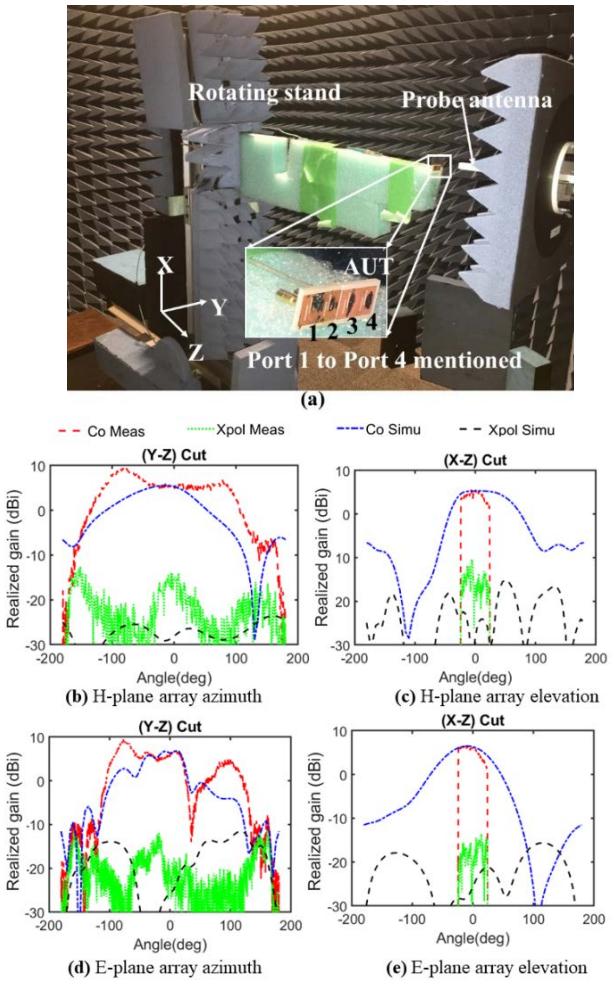

FIGURE 17. (a) The anechoic chamber setup for the 4 element E-plane array embedded element pattern testing; (b-c) simulated and measured embedded element patterns for port 2 of the 4 element H-plane array; (d-e) for port 4 of the 4 element E-plane array. The large maxima at +/- 90 degrees in the measured patterns are caused by radiation from the feed cable behind the antenna. The feed cable is much larger than the array, as can be seen in (a).

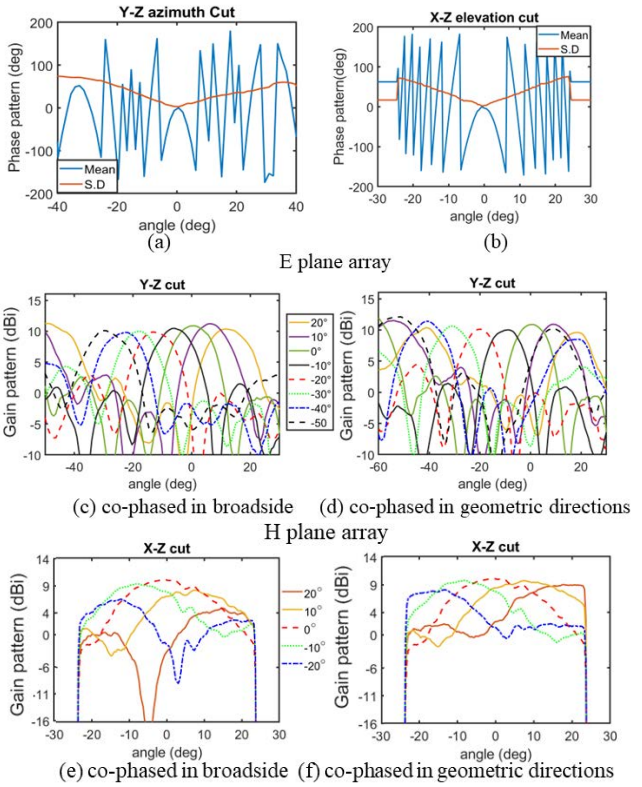

FIGURE 18. Co-pol patterns from measurements.(a-b) mean and standard deviation (S.D)) of phase of E-plane embedded elements after co-phasing of element patterns at broadside; (c) beam-formed E-plane pattern using the measured embedded element patterns phase-aligned at broadside; (d) beam-formed E-plane pattern using the measured embedded element patterns phase-aligned at the geometric beam-steering angle; (e) beam-formed H-plane pattern from the measured embedded patterns co-phased at broadside; (f) beam-formed H-plane pattern from the measured embedded patterns phase-aligned at the geometric beam-steering angle.

off-broadside directions, however the broadside direction is reasonable, and the cross-polar ratios are also reasonable with simulated and measured patterns having a cross-polar ratio of about 30dB. The main difference between simulation and measurement is the presence of lobes in the array endfire directions of the measured patterns. These are caused by the presence of the long feed cable (seen in figure 17a), which is much larger than the antenna and which is not part of the simulation. In (c) and (e), the finite support of the measured elevation pattern - a limitation of the measurement capability - is exposed. The gains over this range of support are a reasonable match between measurement and simulation.

The measured embedded element field patterns are now combined using (1), to demonstrate the beam steering performance of the array. Recall that (1) will always be correct because it does not draw on array theory or modelling that requires assumptions.

The phases of the simulated (measured) embedded element patterns at broadside were 92.869°, 91.491°, 89.652°, 84.579° (-88.6°, -48.1°, -47°, -51.1°). The first element of the measured set has a large (∼40°) phase offset, and this was because it was from a measurement taken on a different day to all the others, with a different set-up. These measured phases are all aligned at broadside in the computer combining of the patterns.

Figure 18(a) depicts the mean and standard deviation of the phases of the embedded elements patterns (co-phased at broadside) in the azimuth plane and (b) in elevation plane.

The co-phasing of the element pattern phases at broadside does not support beamforming beyond about 50° because of the high variance of the far-off-axis element pattern phases.

For better beam-forming gains at off-broadside directions, co-phasing of the element patterns for the geometric beam-steered directions can be deployed using knowledge (look-up table) of the embedded pattern phases in the various directions.

Figure 18(c) shows the E-plane array beam-formed for various beam directions (given in the legend) when the

measured embedded element patterns are co-phased at broadside and then geometrically steered to different directions as in equation (1). The beamforming produces distinctive maximum lobes at angles from 20^0 to -50^0, as compared 30^0 to -45^0 expected from the steering angle. The beam-steering directions are significantly different to that expected from the geometric steering angle because of the differences in the phases of embedded elements' patterns in off-broadside directions.

Figure 18d shows the E-plane array beam steering with the element pattern phases *aligned for the various geometric steering beam directions*. Aligning the element pattern phases in the geometric steering directions, instead of at broadside, creates an extra 1 to 3dB gain. Now the scan angles match with the steering angle because the embedded element phases are aligned in the steered directions.

The array antenna gain (using a computer for phased array combination) is seen to be about 10.7 dBi at broadside.

Standard phased array signal combination shows that the signal gain from 4 elements should be 6 dB above the element gains if all the element gains are the same similar and the phases are aligned before combination. (Note from the previous section, the array antenna excess directivity offers better possibilities.) Here, the gain from the array action is higher than the average embedded element broadside gain (about 4.8 dBi) by 5.9 dB, i.e., close to the expected 6dB, and so we are unable to realize any excess gain from the classical array considerations above.

Figure 18e shows beam-steering of the 4-element H-plane array. Recall the ground-plane is very small: 0.7 λ_0 in the E-plane and $0.7\lambda_0 \times 4 = 2.8\ \lambda_0$ in the H-plane. This is for when the embedded element patterns are co-phased at the broadside direction and geometrically phased as per equation (1). It is shown only for our measurement range of $\pm 25^0$ in the elevation plane (x-z cut). The main lobe of the H-plane array antenna pattern is tilted in azimuth due to the asymmetric ground-plane in the E-plane of the prototype.

The array antenna gain is observed to be at 9.9 dBi in the broadside direction. The average embedded element gain in broadside direction is about 4 dBi, hence the 4-element array action boosts the broadside gain by 5.9 dBi which is again close to the expected 6 dB. The beam-steering to 10^o and 20^o shows an array antenna gain of 8 dBi and 4.6 dBi respectively for co-phased element patterns in broadside. The angle of the beam maxima is less than expected angle of beam directions and this is because the high variance of the phase alignment of the embedded element patterns at off-broadside directions. Better alignment of the steering beam direction (and better gain) will result from co-phasing of element patterns in the steering direction.

Figure 18f shows the beam steering when the element pattern phases are co-phased in the geometric scan directions (i.e., not co-phased at broadside). For this, the array antenna gain in broadside direction stays at 9.9 dBi of course. The beam steered to 10^o and 20^o shows array antenna gain of 9.3 dBi, and 8.8 dBi respectively. So this co-phasing in the scan directions gives an increased gain in the off-broadside scan directions of 1-3 dB, a significant improvement.

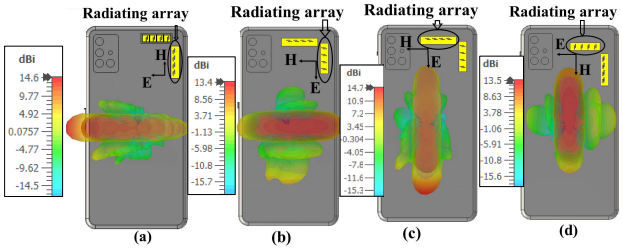

FIGURE 19. Finite arrays on a mobile chassis (a) vertical linear array of horizontal pol (b) vertical linear array of vertical pol (c) horizontal linear array of vertical polarization (d) horizontal linear array of horizontal polarization.

F. CHASSIS MOUNTING

Two finite arrays are mounted on a metallic chassis in various configurations as shown in Figure 19, along with their 3D simulated radiation patterns. Both arrays are assumed to have single independent RF chains and analogue beamforming circuits for each element, as shown in Figure 1 (b). The arrays on the front side (screen side) of the phone, or on the edges, lead to more radiation towards the user's head for call mode. Therefore, we placed the E- and H-plane linear arrays, orthogonally oriented and as closely located as possible, at the *top right corner* of the phone chassis. The top left side of the back of chassis contains a camera and light sensor in this chassis model. At the top right location, the two arrays can provide fan-shaped beams in orthogonal planes. We investigated 4 configurations of E-plane or H-plane arrays with vertical and horizonal polarization, see Figure 19 (a-d). Each array is evaluated in the presence of the other array with terminated elements.

In Figure 19a, a vertical array of horizontally polarized elements has the chassis ground-plane edge in close proximity (about λ_0). Therefore, its main lobe gets tilted in the horizontal plane, as we can expect from the E-plane ground-plane effect on each element, studied above.

Figure 19b depicts a vertically oriented array having vertically polarized radiation. This array has a fan-shaped beam which can be steered in the elevation plane with the analogue phase weights. Figure 19c depicts the beamforming of a horizontally oriented array with vertical polarization. Again, the beam is tilted. Figure 19d shows the horizontal array with horizontal polarization.

Overall, both polarizations work well, but the H-plane arrays continue to exhibit the tilted beams in the E-plane of the antenna element due to the finite ground plane effect.

From these results, the H-plane arrays always suffer from the beam tilt from any ground-plane proximity. Using two E-plane arrays placed orthogonally (not shown in Figure 19) offers the beam-steering in both planes (and in different polarizations) without the beam tilt. If the tilt is a problem, then this latter configuration is the preferred design.

TABLE 3. Performance comparison of reported antenna array with previously published 28 GHz mmWave arrays designs.

Design	Element BW (GHz)	Broadside Gain* (dBi)	Total 3dB Scan Range at 28 GHz	Complexity	Size (mm^3)
This work : (E-plane) (H-plane)	27-29.5 (9%)	12.9 11.2	$+30^0$-45^0, (75^0) $+55^0$-35^0, (90^0)	1 layer PCB antenna through chassis back for both pol	28 × 7 ×1.5
[14] 2020	25.3-29.8 (16%)	12.6	47° to 121° (74^0)	Multi-layer PCB on sides of chassis	32×8×1.2
[12] 2019	24.2–27.5 (13%)	9-11	$\pm35^0$ (at 27.5 GHz)	2-layer PCB inside the metal frame	19.8 × 3.6×0.64
[13] 2020	27.3- 28.2 (3.2%)	12.8	$\pm35^0$ (70^0)	Dual-pol PCB antenna on chassis side frame	32 × 9.5× 0.787
[29] 2019	25-30 (18%)	7	$\pm25^0$ (50^0)	PCB through a side of bezel	23×7×4

V. COMPARISON WITH THE PUBLISHED WORK

With our results now in place, we can compare the performance of our design with that of other published array antennas for 28 GHz. Table 3 summarizes the comparison. Our dual-slot array shows lower bandwidth than previously reported antennas, except [13]. But this bandwidth is easily sufficient for the target standard 5G band of 27.5 to 28. 3 GHz (3%), and in that sense, a wider bandwidth is not improving performance. The broadside gain of our E-plane array is similar, and strictly speaking, greater than the other designs. However, our H-plane design shows a reduced gain by 1.7 dB. The total 3dB scan range of our array is greater than previous reported antennas. It is noted that the 3dB scan of [13] is an extrapolated result (at 27.5 GHz). In summary, our dual-slot arrays give comparative performance to existing designs. The advantage of our design is the much lower complexity and cost of using single-layer PCB for the whole antenna also making its integration with cellphone chassis simpler and less expensive.

VI. CONCLUSION

A simple, low-cost cavity-backed dual-slot antenna element and its 4-element array, arranged in both polarizations, are described along with the design methodology for the configurations. Measurements of prototypes, including their patterns, add practical insights. For the element, the use of a second slot in the cavity significantly increases its -10dB impedance bandwidth from 2.5% to 9%. This extra bandwidth is required for the total active reflection coefficient impedance to cover operation in the standard 5G band of 27.5 GHz to 28.3 GHz, including plenty of room for component and manufacturing tolerances. Classical large-array principles are explored to guide the design, but the resulting ''excess directivity'' of an idealized array is seldom possible to realize in practice due to real-world embedded element patterns being non-identical, and having non-zero mutual coupling. We also explore the available array antenna pattern theories for including mutual coupling, for their applicability for small arrays such as the design presented here. We demonstrate that only one of these theories works well for these small arrays. Finally, a metallic cellphone chassis is modelled to provide a practical platform for the array antennas, and we demonstrate fan-shaped beamforming and beam-steering capability for various array-on-cellphone configuration of orthogonal linear arrays to give both polarizations.

ACKNOWLEDGMENT

The authors acknowledge the materials support of Rogers Corporation for prototype development.

REFERENCES

[1] Y. Yoshimura, ''A microstripline slot antenna,'' *IEEE Trans. Microw. Theory Techn.*, vol. MTT-20, no. 11, pp. 760–762, Nov. 1972.

[2] J. X. Yun and R. G. Vaughan, ''Open slot antenna in small groundplane,'' *IET Microw., Antennas Propag.*, vol. 5, no. 2, pp. 200–213, 2011.

[3] S. A. Long, ''Experimental study of the impedance of cavity-backed slot antennas,'' *IEEE Trans. Antennas Propag.*, vol. AP-23, no. 1, pp. 1–7, Jan. 1975.

[4] F. Paoloni, ''A cavity-backed resonant slot array-theory and measurement,'' *IEEE Trans. Antennas Propag.*, vol. AP-28, no. 2, pp. 259–263, Mar. 1980.

[5] R. Elliott, ''An improved design procedure for small arrays of shunt slots,'' *IEEE Trans. Antennas Propag.*, vol. AP-31, no. 1, pp. 48–53, Jan. 1983.

[6] M. Razmhosseini, R. Zabihi, and R. G. Vaughan, ''Parasitic slot elements for bandwidth enhancement of slotted waveguide antennas,'' in *Proc. IEEE 90th Veh. Technol. Conf. (VTC-Fall)*, Honolulu, HI, USA, Sep. 2019, pp. 1–5.

[7] G. Zhai, Z. N. Chen, and X. Qing, ''Mutual coupling reduction of a closely spaced four-element MIMO antenna system using discrete mushrooms,'' *IEEE Trans. Antennas Propag.*, vol. 64, no. 10, pp. 3060–3067, Oct. 2016.

[8] P. Liu, X.-W. Zhu, Y. Zhang, X. Wang, C. Yang, and Z. H. Jiang, ''Patch antenna loaded with paired shorting pins and H-shaped slot for 28/38 GHz dual-band MIMO applications,'' *IEEE Access*, vol. 8, pp. 23705–23712, 2020.

[9] S. Zhu, H. Liu, Z. Chen, and P. Wen, ''A compact gain-enhanced vivaldi antenna array with suppressed mutual coupling for 5G mmWave application,'' *IEEE Antennas Wireless Propag. Lett.*, vol. 17, no. 5, pp. 776–779, May 2018.

[10] R. S. Brar, R. G. Vaughan, and M. Felipe, ''Phased arrays and MIMO: Wideband 5G end fire elements on liquid crystal polymer for MIMO,'' in *Proc. IEEE Int. Symp. Phased Array Syst. Technol. (PAST)*, Oct. 2019, pp. 1–5.

[11] M. Razmhosseini, A. Bhattacharya, and R. G. Vaughan, "Practical diversity design for PCB IoT terminals," *IEEE Open J. Antennas Propag.*, vol. 1, pp. 627–643, 2020.
[12] R. Rodriguez-Cano, S. Zhang, K. Zhao, and G. F. Pedersen, "Reduction of main beam-blockage in an integrated 5G array with a metal-frame antenna," *IEEE Trans. Antennas Propag.*, vol. 67, no. 5, pp. 3161–3170, May 2019.
[13] H. Li, Y. Cheng, L. Mei, and F. Wu, "Dual-polarized frame-integrated slot arrays for 5G mobile handsets," *IEEE Antennas Wireless Propag. Lett.*, vol. 19, no. 11, pp. 1953–1957, Nov. 2020.
[14] H. Li, Y. Cheng, L. Mei, and L. Guo, "Frame integrated wideband dual-polarized arrays for mm-Wave/sub 6-GHz mobile handsets and its user effects," *IEEE Trans. Veh. Technol.*, vol. 69, no. 12, pp. 14330–14340, Dec. 2020.
[15] B. Yu, K. Yang, C.-Y.-D. Sim, and G. Yang, "A novel 28 GHz beam steering array for 5G mobile device with metallic casing application," *IEEE Trans. Antennas Propag.*, vol. 66, no. 1, pp. 462–466, Jan. 2018.
[16] S. Zhang, I. Syrytsin, and G. F. Pedersen, "Compact beam-steerable antenna array with two passive parasitic elements for 5G mobile terminals at 28 GHz," *IEEE Trans. Antennas Propag.*, vol. 66, no. 10, pp. 5193–5203, Oct. 2018.
[17] R. Rodriguez-Cano, S. Zhang, K. Zhao, and G. F. Pedersen, "Mm-Wave beam-steerable endfire array embedded in a slotted metal-frame LTE antenna," *IEEE Trans. Antennas Propag.*, vol. 68, no. 5, pp. 3685–3694, May 2020.
[18] A. Alkhateeb, O. El Ayach, G. Leus, and R. W. Heath, Jr., "Channel estimation and hybrid precoding for millimeter wave cellular systems," *IEEE J. Sel. Topics Signal Process.*, vol. 8, no. 5, pp. 831–846, Oct. 2014.
[19] J. Bang and J. Choi, "A SAR reduced mm-Wave beam-steerable array antenna with dual-mode operation for fully metal-covered 5G cellular handsets," *IEEE Antennas Wireless Propag. Lett.*, vol. 17, no. 6, pp. 1118–1122, Jun. 2018.
[20] R. Mailloux, "Phased arrays in radar and communication systems," in *Phased Array Antenna Handbook*, 2nd ed. Morristown, NJ, USA: Artech, 2005, pp. 12–15.
[21] D. M. Pozar, "A relation between the active input impedance and the active element pattern of a phased array," *IEEE Trans. Antennas Propag.*, vol. 51, no. 9, pp. 2486–2489, Sep. 2003.
[22] B. A. Arand, A. Bazrkar, and A. Zahedi, "Design of a phased array in triangular grid with an efficient matching network and reduced mutual coupling for wide-angle scanning," *IEEE Trans. Antennas Propag.*, vol. 65, no. 6, pp. 2983–2991, Apr. 2017.
[23] H. A. Abdallah and W. Wasylkiwskyj, "A numerical technique for calculating mutual impedance and element patterns of antenna arrays based on the characteristics of an isolated element," *IEEE Trans. Antennas Propag.*, vol. 53, no. 10, pp. 3293–3299, Oct. 2005.
[24] S. Lee and J. Lee, "Active element pattern and array pattern of patch array antenna including ground edge effect," in *Proc. Int. Symp. Antennas Propag. (ISAP)*, Phuket, Thailand, 2017, pp. 1–2.
[25] D. M. Pozar, "Microwave resonators," in *Microwave Engineering*, Hoboken, NJ, USA: Wiley, 2012, pp. 284–288.
[26] T. Namiki, Y. Murayama, and K. Ito, "Improving radiation-pattern distortion of a patch antenna having a finite ground plane," *IEEE Trans. Antennas Propag.*, vol. 51, no. 3, pp. 478–482, Mar. 2003.
[27] T. Lertwiriyaprapa, C. Phongcharoenpanich, and M. Krairiksh, "Analysis of radiation characteristics of a probe fed rectangular cavity-backed slot antenna with finite-size ground plane," in *Proc. IEEE Antennas Propag. Soc. Int. Symp.*, Salt Lake City, UT, USA, Jul. 2000, pp. 714–717.
[28] R. G. Vaughan and J. B. Andersen, "Antenna principles," in *Channels, Propagations and Antennas for Mobile Communications*, London, U.K.: Institution of Electrical Engineers, 2003, pp. 589–590.
[29] J. Kurvinen, H. Kähkönen, A. Lehtovuori, J. Ala-Laurinaho, and V. Viikari, "Co-designed mm-Wave and LTE handset antennas," *IEEE Trans. Antennas Propag.*, vol. 67, no. 3, pp. 1545–1553, Mar. 2019.

RAJVEER S. BRAR (Graduate Student Member, IEEE) received the B.Tech. degree in electronics and communication engineering from Guru Nanak Dev University, Amritsar, India, in 2013, and the M.Tech. degree in electronics engineering from the Indian Institute of Technology (BHU), Varanasi, India, in 2015. He is currently pursuing the Ph.D. degree in engineering science with Simon Fraser University, Burnaby, BC, Canada.

From 2015 to 2016, he was a Project Engineer with the Metamaterials Laboratory, Department of Electrical Engineering, Indian Institute of Technology, Kanpur, India, where he designed multi-polarization multi-band antennas for communication systems. He interned with Benchmark Electronics, Phoenix, AZ, USA, from 2018 to 2019, and Qualcomm Inc., San Diego, CA, USA, in 2021. His research interests include development of phased array antennas, multiple antennas for MIMO, reflecting surfaces for 5G, and mmWave antennas.

RODNEY G. VAUGHAN (Life Fellow, IEEE) is currently the Sierra Wireless Professor of communications with the Department of Engineering Science, Simon Fraser University (SFU), Burnaby, BC, Canada. His university training was in New Zealand and Denmark. Most of his career has involved industrial development where the value of research ultimately drew him to academia. His research interests include information channels and interplay between communications techniques, signal processing, and physical aspects, including sensors, and propagation and scattering of fields and waves. His current projects include theory, design, and evaluation methods for adaptive antenna systems and adaptive acoustic systems.

He is a 2004 fellow of the BC Advanced System Institute and a URSI Correspondent and continues as the New Zealand URSI Commission B Representative. He is also a Professional Engineer registered (P.Eng.), in BC, Canada. He had chair roles for IEEE conferences. In 2006, he served on the international panel for reviewing the funding and knowledge base for information and communications technology (ICT), in U.K. In 2011, he also served on the international panel for the Canadian Communications Research Centre and the ICT Centre of the CSIRO. He has guest-edited special issues. He has been an Associate Editor of the IEEE TRANSACTIONS ON ANTENNAS AND PROPAGATION. He was a multi-term IEEE Distinguished Lecturer of the Vehicular Technology Society.